Inorganic Chemistry

Article

pubs.acs.org/IC

Defect Structure, Phase Separation, and Electrical Properties of Nonstoichiometric Tetragonal Tungsten Bronze $Ba_{0.5-x}TaO_{3-x}$

Xiaojun Kuang,*[†,‡] Fengjuan Pan,[‡] Jiang Cao,[‡] Chaolun Liang,[§] Matthew R. Suchomel,[∥] Florence Porcher,[⊥] and Mathieu Allix*[#]

[†]Guangxi Ministry-Province Jointly-Constructed Cultivation Base for State Key Laboratory of Processing for Nonferrous Metal and Featured Materials, MOE Key Laboratory of New Processing Technology for Nonferrous Metals and Materials, College of Materials Science and Engineering, Guilin University of Technology, Guilin 541004 People's Republic of China

[‡]MOE Key Laboratory of Bioinorganic and Synthetic Chemistry, State Key Laboratory of Optoelectronic Materials and Technologies, School of Chemistry and Chemical Engineering, Sun Yat-Sen University, Guangzhou 510275, People's Republic of China

[§]Instrumental Analysis and Research Center, Sun Yat-Sen University, Guangzhou 510275, People's Republic of China

[∥]Advanced Photon Source, Argonne National Laboratory, Lemont, Illinois 60439, United States

[⊥]CEA Saclay, Laboratoire Léon Brillouin, F-91191 Gif Sur Yvette, France

[#]UPR3079 CEMHTI, 1D Avenue de la Recherche Scientifique, 45071 Orléans Cedex 2, France and Université d'Orléans, Faculté des Sciences, Avenue du Parc Floral, 45067 Orléans Cedex 2, France

Supporting Information

ABSTRACT: New insight into the defect chemistry of the tetragonal tungsten bronze (TTB) $Ba_{0.5-x}TaO_{3-x}$ is established here, which is shown to adapt to a continuous and extensive range of both cationic and anionic defect stoichiometries. The highly nonstoichiometric TTB $Ba_{0.5-x}TaO_{3-x}$ (x = 0.25−0.325) compositions are stabilized via the interpolation of Ba^{2+} cations and $(TaO)^{3+}$ groups into pentagonal tunnels, forming distinct Ba chains and alternate Ta-O rows in the pentagonal tunnels along the c axis. The slightly nonstoichiometric $Ba_{0.5-x}TaO_{3-x}$ (x = 0−0.1) compositions incorporate framework oxygen and tunnel cation deficiencies in the TTB structure. These two mechanisms result in phase separation within the $0.1 < x < 0.25$ nonstoichiometric range, resulting in two closely related $(TaO)^{3+}$-containing and $(TaO)^{3+}$-free TTB phases. The highly nonstoichiometric $(TaO)^{3+}$-containing phase exhibits Ba^{2+} cationic migration. The incorporation of $(TaO)^{3+}$ units into the pentagonal tunnel and the local relaxation of the octahedral framework around the $(TaO)^{3+}$ units are revealed by diffraction data analysis and are shown to affect the transport and polarization properties of these compositions.

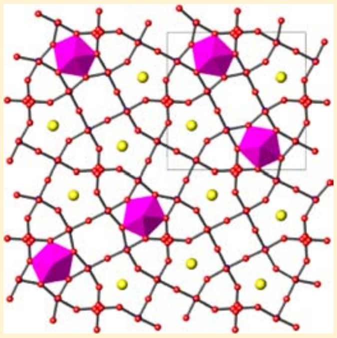

INTRODUCTION

Nonstoichiometry arising from element excess or deficiency is an important component of new materials discovery, representing a powerful strategy that can be used to tailor the structure and properties of crystalline solids.[1−3] This approach may be used to introduce crystallographic point or extended defects[2] (e.g., interstitial/excess oxide ion in $La_{1+x}(Sr/Ca)_{1-x}Ga_3O_{7+0.5x}$ melilite[4,5] and the well-known shear structure in slightly reduced rutile $TiO_{2-\delta}$[3]), or vary charge states in multiple valence cation systems[6] (e.g., Cu^{2+}/Cu^{3+} in cuprate superconductor $Bi_2Sr_2CaCu_2O_{8+\delta}$[7]). Chemical stoichiometry in the tetragonal tungsten bronze (TTB) family has important implications for structure−property correlations in technologically relevant oxide and fluoride TTB compounds that exploit their unique transport,[8] ferroic,[9] and nonlinear optical properties.[10] The basic TTB structure is derived from the perovskite prototype by rotating octahedral units ~45°,[11] forming a corner-sharing octahedral framework penetrated by triangular, square, and pentagonal tunnels of different dimensions that accommodate a range of metal cations.[10] The ideal TTB composition can be described by the general formula $A_4B_2M_{10}X_{30}$, where X is an anion and A, B, and M denote cations in the pentagonal tunnel, square tunnel, and the octahedral sites, respectively. The smallest triangle tunnels are usually empty but can be filled by small cations, such as Li^+.[12] The nonequivalent tunnel sites offer great freedom on controlling the composition/stoichiometry and thus the physical properties of TTB materials.

A number of stoichiometric insulating TTB oxides are interesting candidates for dielectrics and nonlinear optical materials because of polar structures associated with their distorted octahedral framework, such as $Ba_6Ti_2Nb_8O_{30}$ exhibiting both ferroelectricity and high second-harmonic generation (SHG) efficiency.[10] The TTB-related orthorhombic $A_4B_2M_{10}X_{30}$- and $A_4B_{10}M_{18}X_{54}$-type tungsten bronzes are also important for their dielectric properties; examples include the ferroelectric $Ba_4MgTa_{10}O_{30}$[13] and the high permittivity micro-

Received: August 28, 2013
Published: October 29, 2013

dx.doi.org/10.1021/ic402188x | *Inorg. Chem.* 2013, 52, 13244−13252

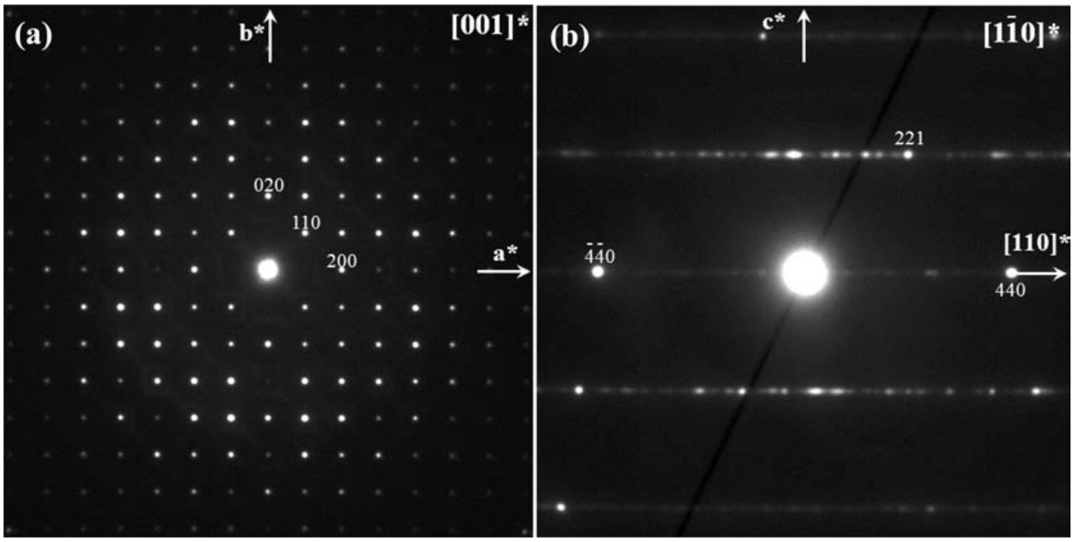

Figure 1. Electron diffraction patterns observed in the $Ba_{0.22}TaO_{2.72}$ sample. (a) Pattern recorded along [001] consistent with the simple TTB cell. (b) [1$\bar{1}$0] pattern showing the diffuse streaks along the [1$\bar{1}$0] direction. The *hkl* indices are labeled in the simple TTB cell.

wave dielectric filters $Ba_{6-3x}Sm_{8+2x}Ti_{18}O_{54}$.[14] The size mismatch of A and B cations in the tunnels and the resulting framework octahedral distortion are responsible for the polarization of the structure, which controls the dielectric properties.[15,16]

Nonstoichiometry in TTB systems is typically observed as A and B site deficiencies in the tunnels,[8] such as seen in the chromatically vibrant and electrically conducting alkali-metal tungsten bronzes Na_xWO_3[8] and the insulating TTB alkali-earth tantalate $Ba_{0.5}TaO_3$.[17,18] A wide range of stoichiometries, i.e., $Ba_{0.5-x}TaO_{3-x}$ (x = 0.125−0.325), were observed in a phase diagram study at 1500 °C of the BaO−TiO_2−Ta_2O_5 ternary system,[19,20] with different crystallographic structures from the simple TTB structure to the $\sqrt{2}$-type and tripled TTB superstructures depending on the composition.[19] Recent investigation of the phase relationship in the BaO−Ga_2O_3−Ta_2O_5 ternary system[21] showed that the TTB solid solution $Ba_{0.5-x}TaO_{3-x}$ in the BaO−Ta_2O_5 binary system extends to x = 0 on the BaO-rich side and adopts the simple TTB cell ($a \sim 12.5$ Å, $c \sim 3.96$ Å) when the materials were fired at 1200 °C. Therefore, $Ba_{0.5-x}TaO_{3-x}$ (x = 0−0.325) represents a TTB system with a unique wide range of nonstoichiometry. In this work, structural analysis of the TTB $Ba_{0.5-x}TaO_{3-x}$ is carried out over the whole solid solution range, and a particularly detailed characterization using a combined refinement of X-ray and neutron diffraction data focuses on the highly nonstoichiometric composition $Ba_{0.22}TaO_{2.72}$ (x = 0.28) synthesized at 1200 °C. From these results, we establish how the defect chemistry in the $Ba_{0.5-x}TaO_{3-x}$ TTB structure adapts to a continuous and extensive range of both cationic and anionic defect stoichiometries. These findings represent important advances of broad significance for tuning the chemical composition, structure, and physical properties of the pentagonal-tunnel-containing octahedral framework family through the exploitation of nonstoichiometric chemical defects.

■ EXPERIMENTAL SECTION

Polycrystalline samples of $Ba_{0.5-x}TaO_{3-x}$ (x = 0−0.35) were synthesized by high-temperature solid-state reaction using $BaCO_3$ (99.99%) and Ta_2O_5 (99.99%) as starting materials, which were weighed according to the aimed stoichiometry and mixed in ethanol. A powder $Ba_{0.22}TaO_{2.72}$ sample of ~8 g for synchrotron powder diffraction (SPD) and constant wavelength neutron powder diffraction (NPD) was prepared by firing the powder at 1200 °C for 24 h with an intermediate grinding. The other powder samples in the TTB $Ba_{0.5-x}TaO_{3-x}$ solid solution were fired at 1200−1250 °C for 48−72 h with several intermediate grindings. The $Ba_{0.22}TaO_{2.72}$ pellet for the AC impedance spectroscopy measurement was cold isostatically pressed under a pressure of ~200 MPa, and then fired at 1600 °C for 2 h. The resulting pellet reached only 76% of the theoretical X-ray density because of its low sinterability.

The AC impedance spectra were also measured on the TTB $Ba_6GaTa_9O_{30}$ and $Ba_{0.4}TaO_{2.9}$ (x = 0.1) pellets for comparison. The synthesis of these samples used the starting materials $BaCO_3$, Ta_2O_5, and Ga_2O_3 (99.99%), which were weighed according to the stoichiometries and mixed in ethanol. The mixtures for the $Ba_{0.4}TaO_{2.9}$ and $Ba_6GaTa_9O_{30}$ were calcined at 1000 °C for 12 h and at 1200 °C for 12 h, respectively, and were pressed into pellets. The $Ba_{0.4}TaO_{2.9}$ pellet was fired at 1500 °C for 2 h, affording to reach only ~73% relative density for the pellet. The $Ba_6GaTa_9O_{30}$ pellet was fired at 1450 °C for 12 h, leading to a dense pellet of ~93% relative density.

The phase assemblages were examined by laboratory X-ray powder diffraction (XRD) using a Bruker D8 ADVANCE powder diffractometer operating with Cu Kα radiation at 40 kV and 40 mA. High-intensity and high-resolution SPD data were collected on the 11-BM diffractometer at the Advanced Photon Source (APS), Argonne National Laboratory. The sample powder was loaded in a 0.3 mm diameter glass capillary, and data were collected at room temperature over the 1−60° 2θ range using a step size of 0.001° and wavelength of λ = 0.413957 Å. The sample was spun at 10 Hz to improve powder averaging of the crystallites. NPD data were measured at room temperature on the 3T2 diffractometer (Laboratoire Léon Brillouin, France) using wavelength λ = 1.2255 Å on approximately 8 g of sample over the 4.5−121° (2θ range) with a 0.05° step size. Electron diffraction (ED) experiments were performed on a Philips CM20 transmission electron microscope (TEM) fitted out with an Oxford EDS analyzer. The sample was first crushed in ethanol, and a drop of the suspension with the small crystallites was deposited onto a carbon-coated copper grid.

The Rietveld analysis[22] of the $Ba_{0.22}TaO_{2.72}$ structure was carried out using the Topas Academic[23] and Jana2006[24] software on both XRD and NPD data. The x dependency of cationic distributions over the square and pentagonal tunnels in the TTB $Ba_{0.5-x}TaO_{3-x}$ solid solution was examined by Rietveld refinement of the laboratory XRD data. Bond valence sums (BVSs) were calculated by Brown and Altermatt's method.[25]

Density measurements were conducted on an ACCUPIC 1330 (Micromeritics) gas picnometer running under helium at a temperature of 30 °C ± 1 °C. Optical SHG coefficient measurements were performed on powder samples by means of the Kurtz-Perry method with 1064 nm light generated with a Q-switched Nd:YAG laser using the KH_2PO_4 powder samples as a reference.

AC impedance spectroscopy (IS) measurements were performed with a Solartron1260A impedance/gain-phase analyzer over 10^{-1}–10^{7} Hz from room temperature to 900 °C. Prior to the IS measurement, the pellets were coated with platinum paste and fired at 800 °C for 30 min to burn out the organic components in order to form dense electrodes. The measured capacitance from the impedance data was corrected for permittivity calculations by subtracting the blank contribution arising from the sample holder and connection cables, which was measured on an open circuit without the pellet. Impedance measurements of $Ba_{0.22}TaO_{2.72}$ were performed under O_2 and N_2 gas flows to examine whether the electrode response in impedance data changes with the oxygen partial pressure, which provides information about possible oxide ion conduction in the $Ba_{0.22}TaO_{2.72}$ ceramic.

■ RESULTS

Structure of $Ba_{0.22}TaO_{2.72}$ (x = 0.28). TEM examination confirmed that the majority of the $Ba_{0.22}TaO_{2.72}$ sample produced at 1200 °C adopts the simple TTB cell (Figure1a) and revealed the presence of inhomogeneous local ordering, exhibiting different types of TTB superstructures and varying nature from one crystallite to another (Figure S1a,b in the Supporting Information). Figure 1b shows, for example, diffuse streaks along the $[1\bar{1}0]$ direction. This implies potential ordering along the $\langle 110\rangle$ direction, consistent with the $\sqrt{2}$-type superstructure[19] reported by Vanderah et al. for the material fired at higher temperatrue (1500 °C). Figure S1a,b shows ordering along the *a* axis, indicating the presence of two superstructures with 3-fold and 6-fold *a* axes, respectively.

The complexity of the ordering observed prevented an unambiguous TTB superstructure determination. Therefore, preliminary Rietveld analysis was performed on the laboratory XRD data using the simple TTB cell in the centric *P*4/*mbm* space group (the SHG measurement did not detect the apparent SHG effect in the $Ba_{0.22}TaO_{2.72}$ sample, which confirms the appropriate centric space group choice). In the *P*4/*mbm* centric model (Figure 2), there are one A site (4*g*) located in the pentagonal tunnel and one B site (2*a*) in the square tunnel, two octahedral Ta sites, Ta1 (2*c*), which is coordinated by two O1 (2d), and four O4 (8*j*), and Ta2 (8*j*), which is coordinated by one O4, one O2 (4*h*), two O3 (8*i*), and two O5 (8*j*). The site occupancies on square and pentagonal tunnels were refined against the laboratory XRD data, which showed that the A sites (4*g*, *x*, *x* + 0.5, 0) in the pentagonal tunnels are partially occupied by Ba (~66.5(4)% with the B_{iso} value fixed at 1 Å^2) and the square tunnels are empty (0.003(5) Ba at the B site). This resulted in reliability factors R_{wp} ~ 15.5% and R_B ~ 12.8%. Difference Fourier map calculation was performed, which showed a residual peak at a 4*h* site (~0.33, ~0.17, 0.5), ~2 Å apart from the Ba site in the pentagonal tunnels (Figure S2, Supporting Information). A Ta atom was placed on this new crystallographic site (Ta3), and its refined occupancy is ~29.6(3)% (with the B_{iso} value fixed at 1 Å^2). This improved the fit significantly (R_{wp} ~ 8.07% and R_B ~ 2.55%). The Ta atoms in the pentagonal tunnels appear 5-coordinated and under-bounded (BVS of Ta3 is ~2.8). This requires simultaneous occupation of oxygen atoms on the remaining A sites (i.e., the Ba 4*g* sites) in the pentagonal tunnels to form a 7-coordinated geometry environment for the Ta atoms to meet the chemical bonding requirement of Ta^{5+}. In other words, chains composed of alternating Ta^{5+} and O^{2-} species (referred to as $(TaO)^{3+}$ units) enter into the pentagonal tunnels, similar to the case of $M_8W_9O_{47}$ (M = Nb, Ta), where two-thirds of the pentagonal tunnels are empty and $(MO)^{3+}$ groups enter the remaining pentagonal tunnels.[26,27]

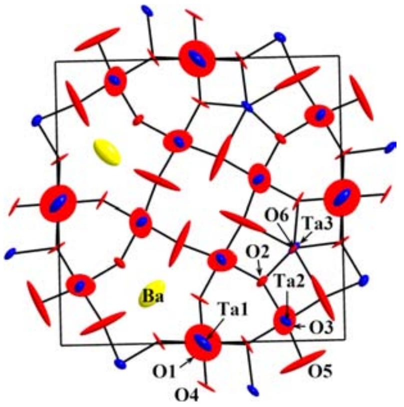

Figure 2. View of the average $Ba_{0.22}TaO_{2.72}$ structural model showing the anisotropic displacement parameters (ellipsoids drawn with a 99% probability). For each pentagonal tunnel, only one Ba^{2+} or $(TaO)^{3+}$ species is represented for clarity.

High-resolution SPD data and NPD data were then used for elucidating the defect structure of $Ba_{0.22}TaO_{2.72}$. The SPD data can be well-fitted with the simple TTB tetragonal cell and do not show any evidence for low symmetry cells. The neutron scattering lengths (fm) for Ba, Ta, and O are 5.07, 6.91, and 5.803, respectively.[28] The Ba and O at the mixed occupied sites can be discerned clearly using a combined Rietveld analysis on both the SPD and the NPD data because of the sensitivity of XRD to the heavy Ba atoms and the significant neutron scattering contribution of O atoms comparable to Ba atoms. The combined refinement confirmed that the 4*g* Ba sites in the pentagonal tunnels comprise oxygen in addition to Ba, and their refined occupancies were found to be 36.0(5)% for oxygen and 62.6(1)% for Ba. The refined oxygen occupancy was close to that for the Ta (31.0(1)%), consistent with the proposed $(TaO)^{3+}$ as a group entering the pentagonal tunnels. Thus, the occupancies of Ta and O in the pentagonal tunnels were constrained to be identical during the next refinement cycles. Finally, the refined occupancies of $(TaO)^{3+}$ units and Ba^{2+} atoms in the pentagonal tunnels are 30.8(1)% and 65.4(1)%, respectively.

The refinement shows that isotropic displacement factors B_{iso} for sites O1 (linking the $Ta1O_6$ octahedra along the *c* axis) and O5 (defining the square tunnels) are as large as ~2.8 and ~3.4 Å^2, respectively. Refinement of anisotropic displacement factors (ADPs) for all modeled atoms improved the fit significantly (R_{wp} ~ 2.25% (NPD) and ~ 8.11% (SPD) versus R_{wp} ~ 4.80% (NPD) and ~ 8.89% (SPD) using isotropic displacement factors). The refined structural parameters for $Ba_{0.22}TaO_{2.72}$ in the average structural model using the ADPs are provided in Table S1 (Supporting Information). The large sizes and shapes of the ellipsoids for sites O1 and O5 in Figure 2, representing their refined ADPs, suggest positional disorder for sites O1 and O5. The isotropic displacement factors of O5 can be reduced by using a lower symmetry structural model, for example, the noncentric *P*4*mb* space group. However, a lower symmetry model does not result in a reduced displacement factor for O1, even when the symmetry was reduced to *P*4. The ADPs of O1 indicated the positional disorder within the *ab* plane for O1, which means that a more general site is required to describe correctly O1. Moving O1 off to a general site (16*l*) from the original 2*d* site is helpful on reducing the B_{iso} value, and the position fraction refinement led to an 8*i* site for O1 finally with 25% occupancy. The O5 ellipsoids display elongation toward the centers of the pentagonal and square tunnels, which implies local relaxation of the oxygen framework around the $(TaO)^{3+}$ defect units in the pentagonal tunnels. The Ta^{5+} atoms in the pentagonal tunnels appear under-bonded in the average structural model (BVS of Ta3 is 4.27).

To model the local relaxation arising from the incorporation of $(TaO)^{3+}$ units into the pentagonal tunnels, a site-split model was considered and refined by partially displacing the O5 site (8*j*) to a neighboring $O5_L$ site (8*j*) corresponding to the $(TaO)^{3+}$ units in the pentagonal tunnels (the original O5 site corresponds to the Ba^{2+} cation in the pentagonal tunnels for the bulk structure). The refinement showed that $O5_L$ is locally displaced from O5 by ~0.54 Å toward Ta^{5+} in the pentagonal tunnels, which increased the BVS of Ta^{5+} in the pentagonal tunnels to 4.87, providing a satisfactory chemical bonding environment for $(TaO)^{3+}$ defect units (the BVS of O6 in $(TaO)^{3+}$unit is 1.81). All the site occupancies were refined subject to the charge neutrality constrained by a simulated annealing approach[29] using Topas Academic software at the final stage. The refined composition for $Ba_{0.22}TaO_{2.72}$ is $Ba_{2.643(5)}(TaO)_{1.250(3)}Ta_{10}O_{29.56(2)}$ (in unit cell) with a calculated density of 7.840(3) g/cm^3. This is slightly lower than the measured density of 7.876(9) g/cm^3 (for the same sample used for the NPD), but it is in a reasonable agreement with the experimental value given that the site occupancy is highly correlated with atomic displacement factors. The final refinement of the site-split model converged to R_{wp} ~ 3.44%, R_B ~ 1.95% for NPD data and R_{wp} ~ 8.86%, R_B ~ 3.79% for SPD data. The Rietveld plots of the SPD and NPD data are shown in Figure 3. The final refined structural parameters for the site-split model are listed in Table 1. The selected interatomic distances are listed in Table S2 (Supporting Information), and the bond angles in the TaO_n polyhedron are listed in Table S3 (Supporting Information).

Phase Separation in the TTB $Ba_{0.5-x}TaO_{3-x}$. Following the structural determination of the defect $Ba_{0.22}TaO_{2.72}$ TTB structure, we used laboratory XRD data to perform careful examination of the phase formation in the $Ba_{0.5-x}TaO_{3-x}$ ($x \geq 0$) material fired at 1200−1250 °C. The results show that the TTB $Ba_{0.5-x}TaO_{3-x}$ system does not form a continuous single solid solution. Instead, the TTB $Ba_{0.5-x}TaO_{3-x}$ system can be divided into three regions: (i) a single tetragonal phase (T1) in the $x = 0$−0.1 range, (ii) a single tetragonal phase (T2) for $x =$ 0.25−0.325, and (iii) a mixed T1 and T2 phases for $0.1 < x <$ 0.25.

Two-phase Rietveld analysis was performed for the mixture materials, and the simple TTB *P*4/*mbm* space group was employed for both T1 and T2 phases, although the real symmetry for the T1 solid solution phase could be lower, such as the commonly found polar *P*4*bm* or the nonpolar $P\bar{4}b2$ proposed by Vanderah et al.[19] Figure 4 shows the Rietveld refinement plots of the XRD pattern for the $x = 0.17$ sample, which demonstrates that using a single TTB phase leads to a rather poor fit of the XRD pattern and that a two TTB phases model improved the Rietveld refinement significantly. The $\sqrt{2}$-type and tripled TTB superstructures[19] have been also considered and were tried for the Rietveld and Pawley refinements. None of these alternatives accounted for all the reflections and gave good fits to the XRD data, excluding the possibility of formation of the ordered superstructures. Quenching the mixed T1 and T2 phase samples from 1200 °C to room temperature did not result in single TTB phase materials, and the phase mass contents in the mixtures were not affected by the quenching at all.

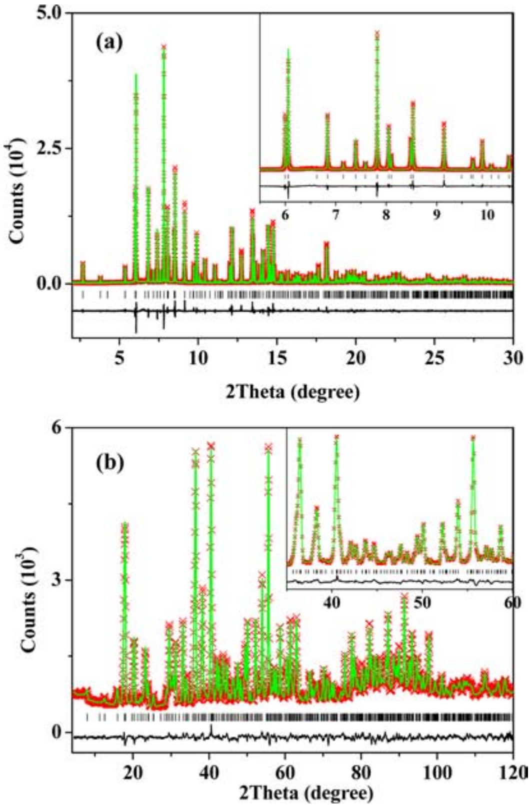

Figure 3. Rietveld refinement of SPD (a) and NPD (b) data for $Ba_{0.22}TaO_{2.72}$. The Bragg reflection positions are shown by tick marks. The insets in (a) and (b) enlarge the plots in the 2θ ranges of 5.5−10.5° in SPD data and 35−60° in NPD data, respectively.

The Rietveld refinement showed that the pentagonal tunnels in the T1 and the T2 phases are (TaO)-free and (TaO)-containing, respectively. The *x* dependency of cationic distributions over the square and pentagonal tunnels is shown in Figure 5a. In the mixed T1 and T2 phase materials, the refined cell volumes (Figure 5b) for the T1 and T2 phases remain essentially unchanged over the phase separation region. The cell volume of phase T1 is larger than that for phase T2 (616.05(2) Å^3 for phase T1 versus 613.06(3) Å^3 for phase T2 in sample $x = 0.17$). Such a gap between the cell volumes was preferably ascribed to the smaller *c* axis of the T2 phase (3.91577(8) Å versus the *c* axis 3.93071(6) Å for the T1 phases), as the difference between the *a* axes for the T1 (12.5191(2) Å) and T2 (12.5125(2) Å) phases is only about half of that between the *c* axes of the T1 and T2 phases.

Electrical Properties of the TTB $Ba_{0.5-x}TaO_{3-x}$. The complex impedance plot at 345 °C for the $Ba_{0.22}TaO_{2.72}$ pellet comprises a large semicircular arc for the bulk response, a small semicircular arc for the grain boundary response, and a Warburg-type electrode response (Figure 6a). The bulk response can be modeled with parallel resistor (*R*) and capacitor (*C*) elements, and the bulk resistivity (R_b) for the $Ba_{0.22}TaO_{2.72}$ pellet was estimated as the intercept of the large semicircular arc at low frequency, and the associated

Table 1. Final Refined Structural Parameters of $Ba_{0.22}TaO_{2.72}$ in the Site-Split Model[a]

atom	site	x	y	z	occupancy	B_{iso} (Å^2)	BVS[b]
Ba	4g	0.17595(7)	0.67595(7)	0	0.661(1)	1.79(3)	1.90
Ta1	2c	0	0.5	0.5	1	1.18(1)	5.48
Ta2	8j	0.06974(2)	0.20687(2)	0.5	1	0.653(3)	5.18
Ta3	4h	0.32706(8)	0.17294(8)	0.5	0.313(1)	1.15(3)	4.87
O1	8i	0.0228(3)	0.5033(3)	0	0.249(1)	0.70(7)	1.91
O2	4h	0.28792(7)	0.78792(7)	0.5	0.959(2)	0.74(3)	1.98
O3	8i	0.0740(1)	0.21147(9)	0	0.990(1)	1.62(2)	1.86
O4	8j	0.34499(9)	0.00832(8)	0.5	0.990(1)	1.17(2)	2.26
O5	8j	0.1369(2)	0.0682(2)	0.5	0.668(1)	1.81(3)	1.96
O5$_L$	8j	0.1757(2)	0.0870(3)	0.5	0.319(1)	0.22(5)	2.00
O6	4g	0.1755(3)	0.6755(3)	0	0.313(1)	0.38(7)	1.81

[a] R_{wp} ~ 3.44%, R_B ~ 1.95% for NPD data; R_{wp} ~ 8.86%, R_B ~ 3.79% for SPD data. [b] The site occupancies are considered in the BVS calculation.

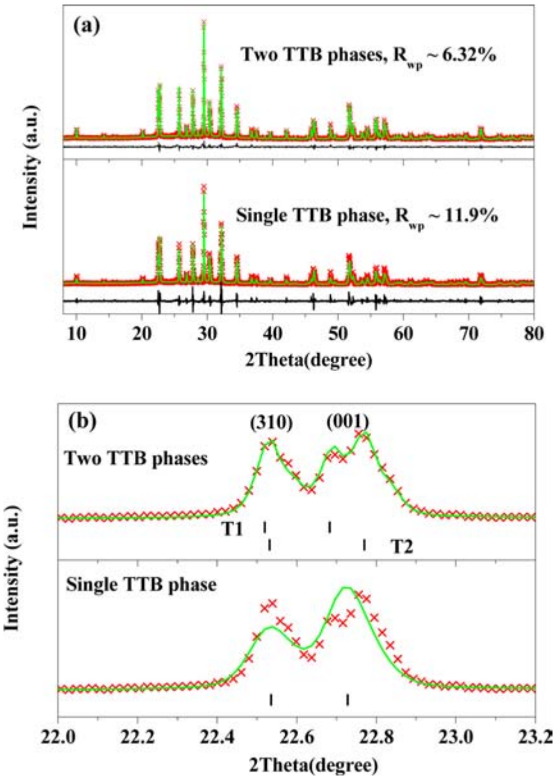

Figure 4. Comparison of the Rietveld refinements of the XRD pattern for the $x = 0.17$ sample in $Ba_{0.5-x}TaO_{3-x}$ using either a single TTB phase or a two TTB phases model. The plots corresponding to the (310) and (001) reflections are enlarged in (b). T1 and T2 denote the tetragonal TTB phases without and with the $(TaO)^{3+}$ units in the pentagonal tunnels, respectively. The refined mass percentages for the T1 and T2 phases are 57.9(3)% and 42.1(3)%, respectively. The vertical marks in (b) denote the reflection positions.

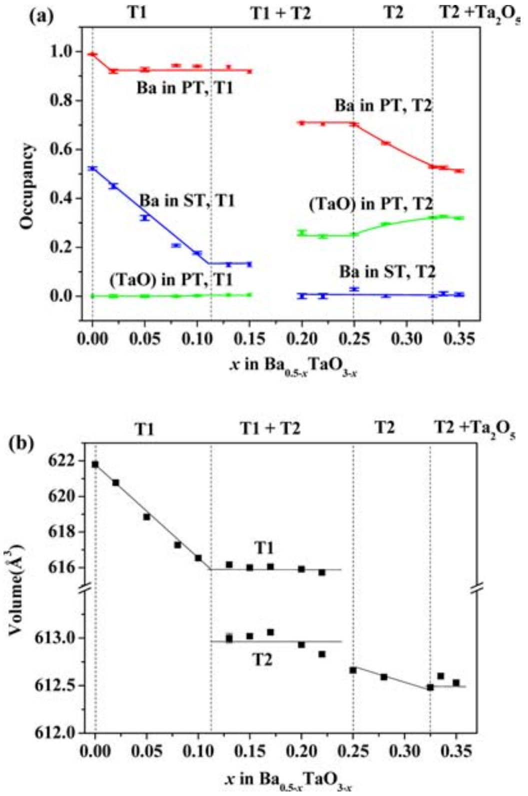

Figure 5. Refined cationic compositions (a) in the square tunnel (ST) and pentagonal tunnel (PT) and the refined cell parameters (b) as functions of x in the TTB $Ba_{0.5-x}TaO_{3-x}$ solid solution. T1 and T2 denote the TTB phases without and with the $(TaO)^{3+}$ units in the pentagonal tunnels, respectively. The phase boundaries are shown by the vertical dashed lines, and the phase nature of each region is given in the top of the figure. Mixed T2 and Ta_2O_5 phases form in the region between $0.325 < x < 0.5$.

capacitance calculated using the equation $\omega RC = 1$ (ω is angular frequency, $2\pi f_{max}$, where f_{max} is the frequency corresponding to the maximum Z'') is ~5 pF/cm, consistent with the bulk response.[30] The electrode response gradually collapsed down to a semicircular arc with increasing temperature (Figure 6b), displaying high capacitance (10^{-8}–10^{-6} F/cm) in the low-frequency range, indicative of ionic conduction.

The impedance data at 591 °C for the $Ba_{0.4}TaO_{2.9}$ pellet comprise the bulk response corresponding to the large semicircular arc and the grain boundary response corresponding to a small tail in the low-frequency region (in Figure 6c). The impedance data of the $Ba_6GaTa_9O_{30}$ pellet at 691 °C is composed of a single semicircular arc, which can be ascribed to the bulk response (Figure 6d) with associated capacitance ~ 9 pF/cm. No significant grain boundary and electrode response contributions were observed in the impedance data of the $Ba_6GaTa_9O_{30}$ pellet. The Arrhenius plots of TTB $Ba_{0.22}TaO_{2.72}$, $Ba_{0.4}TaO_{2.9}$, and $Ba_6GaTa_9O_{30}$ are shown in Figure 7. The dielectric permittivities of $Ba_{0.22}TaO_{2.72}$ and $Ba_{0.4}TaO_{2.9}$ pellets were calculated from the impedance measurement, and their ambient temperature permittivities are ~46 and ~60 at 1 MHz, respectively.

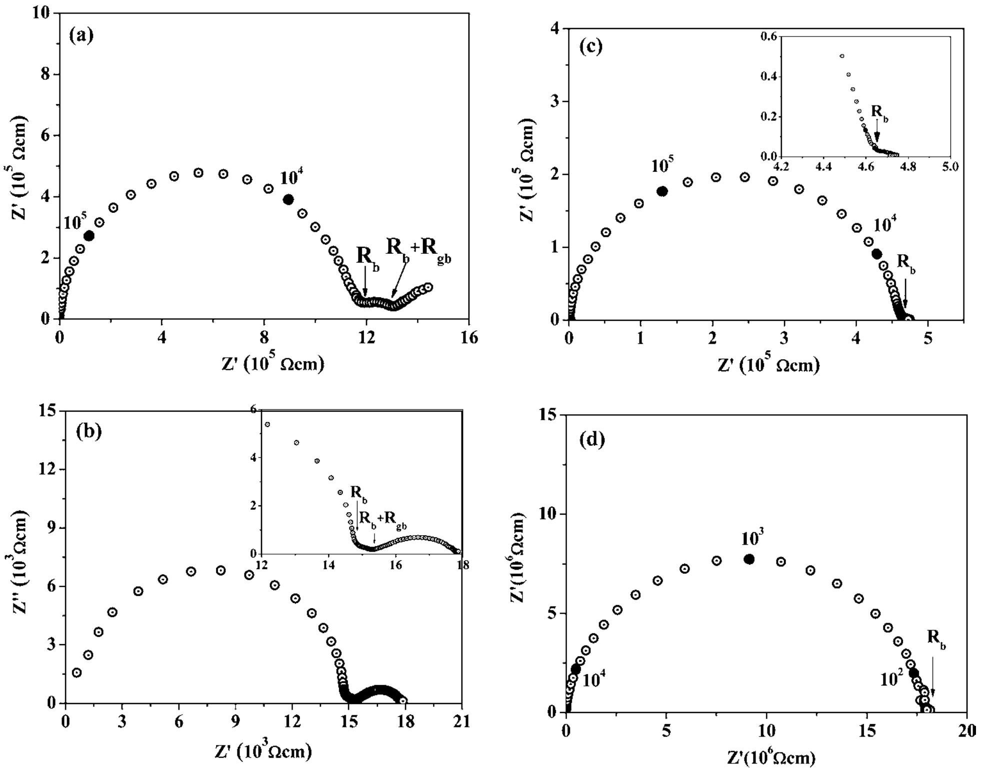

Figure 6. Complex impedance plots for the $Ba_{0.22}TaO_{2.72}$ at 345 °C (a) and 744 °C (b), $Ba_{0.4}TaO_{2.9}$ at 591 °C (c), and $Ba_6GaTa_9O_{30}$ at 691 °C (d). The numbers label the selected frequencies (Hz) marked by filled circles. R_b and R_{gb} denote bulk and grain boundary resistivities, respectively. The insets in (b) and (c) enlarge the plots in low-frequency regions to show grain boundary responses clearly. The low-frequency small tail in (c) is ascribed to grain boundary response.

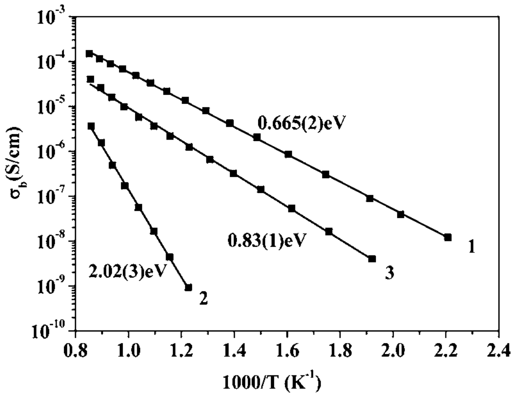

Figure 7. Arrhenius plots of the bulk conductivities of TTB $Ba_{0.22}TaO_{2.72}$ (1), $Ba_6GaTa_9O_{30}$ (2), and $Ba_{0.4}TaO_{2.9}$ (3). The numbers denote the activation energies for these three samples.

■ DISCUSSION

The incorporation of $(TaO)^{3+}$ units into the pentagonal tunnels in $Ba_{0.22}TaO_{2.7}$ results in two distinct chains of $(TaO)^{3+}$ units and Ba^{2+} cations locally in the pentagonal tunnels along the *c* axis. ED patterns and Rietveld analysis show that a majority of $(TaO)^{3+}$ rows and Ba^{2+} chains in the pentagonal tunnels are distributed in a disordered manner in $Ba_{0.22}TaO_{2.72}$ fired at 1200 °C. The alternation of Ta and O in the pentagonal tunnels forms isolated one-dimensional corner-sharing single 7-coordinated pentagonal-bipyramidal $Ta3O_7$ chains along the *c* axis (Figure 8a,b). The incorporation of $(TaO)^{3+}$ units into the pentagonal tunnels results in local displacement of O5 toward the tunnel centers, which, in turn, leads to the expansion of the neighboring empty square tunnels (Figure 8a), which is predicated to be favorable for electrochemical intercalation.[31] Another consequence of the incorporation of the $(TaO)^{3+}$ units into the pentagonal tunnels is the distortion of four O5-bridged $Ta2O_6$ octahedra within the five octahedra defining the 5-fold ring. This may rend the four nearest neighboring pentagonal tunnels isolated by the $Ta2O_6$ octahedra unfavorable for the accommodation of $(TaO)^{3+}$ units. Thus, the local favorable $Ta2O_6$ octahedral framework around the defect $Ta3O_7$ chain in the pentagonal tunnels is bridged by $O5_L$ (Figure 8a,c), in contrast with the O5 bridging the $Ta2O_6$ octahedra around the neighboring pentagonal tunnels occupied by Ba^{2+} cations.

No apparent Ta atoms were observed in the pentagonal and square tunnels in the T1 phase, which indicates that the nonstoichiometric TTB $Ba_{0.5-x}TaO_{3-x}$ is stabilized by accommodating the Ba and O deficiency as oxygen vacancies (~ ≤ 3.3%) and A(B)-site vacancies (~ ≤ 33%) in the $x = 0-0.1$ range. The formula of phase T1 can be described as $[Ba]_{1-y}(Ba)_{4-z}Ta_{10}O_{30-y-z}$, where [ ] and ( ) represent the square and pentagonal tunnels, respectively, and the sum of *y* and *z* is 10 times the *x* value in $Ba_{0.5-x}TaO_{3-x}$. The TTB T2 phase is stabilized with higher Ba and O deficient nonstoichiometry in $Ba_{0.5-x}TaO_{3-x}$ (in $0.25 \leq x \leq 0.325$ range), requiring that the pentagonal tunnels are filled with $(TaO)^{3+}$ rows to reduce the number of the empty tunnels as well as the framework oxygen vacancies. A $[Ba]_0(Ba)_{4-y}(TaO)_zTa_{10}O_{29-y+1.5z}$ formula ($z \leq y$; [ ] and ( ) represent the square and pentagonal tunnels, respectively) can be used to describe the T2 TTB phase (for $Ba_{0.22}TaO_{2.72}$, $y = 1.357$, $z = 1.250$ according to the refinement). Given the empty square tunnel in the T2 phase, the framework oxygen vacancies appear

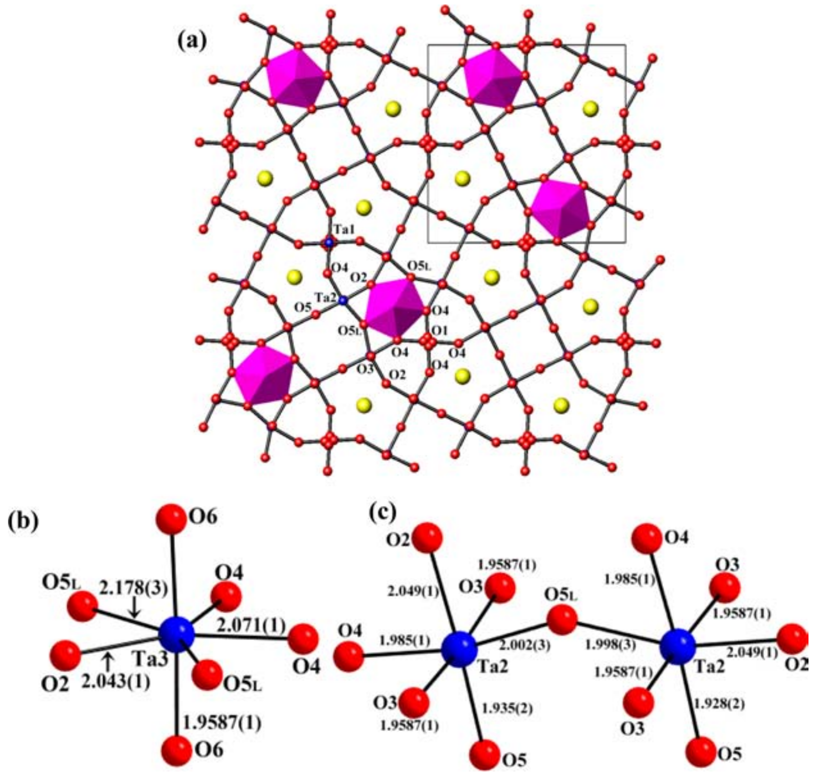

Figure 8. (a) Schematic plot of the defect TTB $Ba_{0.22}TaO_{2.72}$ structure, illustrating one example of local distribution of $(TaO)^{3+}$ (31.25%) and Ba^{2+} (68.75%) over the pentagonal tunnels, which shows that the five nearest neighboring pentagonal tunnels around the corner-sharing TaO_7 chain (in pink) are occupied by Ba^{2+} cations (in yellow). Some of the O1 and O3 atoms above the respective Ta1 and Ta2 atoms (in blue) are removed for more clarity. O1 sites are partially occupied. Representation of (b) the pentagonal-bipyramidal $Ta3O_7$ and (c) the local $Ta2O_6$ octahedra linkage by $O5_L$ around the defect $Ta3O_7$ chain in the pentagonal tunnels. The two O5 atoms in (c) are from two different neighboring pentagonal tunnels occupied by Ba^{2+} cations. The numbers denote the bond lengths (Å).

imperative for stabilizing this defected TTB structure because the structure with empty square tunnels and free of oxygen vacancies could be accessible only in the $y \geq 2$ range of $[Ba]_0(Ba)_{4-y}(TaO)_{(2+2y)/3}Ta_{10}O_{30}$, i.e., the compositions beyond $Ba_{1/6}TaO_{2.5+1/6}$ having a content of $(TaO)^{3+}$ exceeding the maximum limits (1/3), which otherwise form mixtures of the T2 and Ta_2O_5 phases.

In contrast with the phase separation found in the multiferroic TTB fluoride $K_{0.58}FeF_3$, presumably associated with the potassium content separation,[32] the phase separation seen here in $Ba_{0.5-x}TaO_{3-x}$ leads to two distinct, but closely related, $(TaO)^{3+}$-free (T1) and $(TaO)^{3+}$-containing (T2) TTB phases, suggesting that it is thermodynamically unfavorable to dilute $(TaO)^{3+}$ units in the pentagonal tunnels to form a single TTB phase in the $0.1 < x < 0.25$ range. This suggests that a spontaneous composition separation process occurs. As revealed by the site-split refinement, the incorporation of $(TaO)^{3+}$ into pentagonal tunnels results in octahedral distortion and atomic displacement, which could lead to different symmetries for the T1 and T2 phases. Determining the symmetry for the T1 phase is not in the scope of this study.

The contents of $(TaO)^{3+}$ units and Ba^{2+} cations in the pentagonal tunnels are variable over the T2 solid solution region (Figure 5a), and the content of the $(TaO)^{3+}$ units varies within the 25.3(4)−32.6(5)% range, compared to the narrower 29−33% range occurring in the TTB niobium and tantalum tungsten oxides with the composition $M_{34}O_{94}$ (~33%, M can be Nb, Ta, or W) and the metastable phases (~29−30%) in the oxidation products of some mixed-valent members,[33] where the $(MO)^{3+}$ groups entering ≤1/3 of pentagonal tunnels and the remaining pentagonal tunnels are empty (e.g., in $Nb_{16}W_{18}O_{94}$) or can be partially occupied by large cations (e.g., in $Bi_6Nb_{34}O_{94}$).[27,33] This makes $Ba_{0.5-x}TaO_{3-x}$ ($x = 0.25-0.325$) a thermal-stable defected TTB example with a tunable content of the alternate metal−oxygen arrays in the pentagonal tunnels. It can be concluded that the maximum number of $(MO)^{3+}$ groups entering in the TTB structure is 1/3, lower than the 1/2 value observed on the related orthorhombic $A_4B_2M_{10}X_{30}$-type tungsten bronze $NaNb_6O_{15}F$.[34]

The refined occupancies for the framework oxygen sites O1−O5 in $Ba_{0.22}TaO_{2.72}$ display vacancies varying within the range of ~1−4%, leading to a total oxygen vacancy concentration ~1.5% over the framework oxygen sites. To determine whether the mobile species in the $Ba_{0.22}TaO_{2.72}$ ceramic are oxygen ions, we performed impedance measurement under O_2 and N_2 flows. Typically, oxygen diffusion and charge transfer reactions taking place at the interface among the oxide ion conducting material, electrode, and atmosphere are strongly dependent on the partial oxygen pressure. In this scenario, the electrode response associated with oxide ion conduction should display higher impedance, or even revert back to a Warburg-type impedance response from a semicircular arc at high temperature once the atmosphere changed from O_2 to N_2. However, no significant correlation was observed in this study between the electrode responses in O_2 to N_2 atmospheres, indicating that the oxygen vacancies in the octahedral framework have little contribution to the conductivity of the $Ba_{0.22}TaO_{2.72}$ ceramic. This agrees well with the observation that the (TaO)-free T1 phase

$Ba_{0.4}TaO_{2.9}$ pellet (containing ~3% framework oxygen vacancies) exhibits conductivity an order of magnitude lower (Figure 7) than that for $Ba_{0.22}TaO_{2.72}$ (containing ~1.5% of framework oxygen vacancies). Therefore, we can conclude that the origin of the ionic conduction observed in $Ba_{0.22}TaO_{2.72}$ should be attributed to the Ba^{2+} migration in the tunnels. Such Ba^{2+} cationic conduction has been observed previously in the Ba^{2+}-containing β-alumina material.[35] Given the nearly fully occupied pentagonal tunnels and empty square tunnels in $Ba_{0.22}TaO_{2.72}$, the preferable Ba^{2+} migration pathways involve intertunnel hopping between the square and pentagonal tunnels, consistent with the elongation of the Ba^{2+} cation ellipsoids in the pentagonal tunnels toward the square tunnels (Figure 2), followed by intratunnel hopping inside the square (or pentagonal) tunnels. In contrast with the $Ba_{0.22}TaO_{2.72}$ pellet, no apparent electrode response can be discerned for the T1 phase $Ba_{0.4}TaO_{2.9}$ pellet, indicating limited Ba^{2+} cationic motion in $Ba_{0.4}TaO_{2.9}$ despite the fact that 83% of the B sites in the square tunnels of $Ba_{0.4}TaO_{2.9}$ are vacant (Figure 5a), in contrast with the completely vacant square tunnels found in $Ba_{0.22}TaO_{2.72}$. This implies that the long-distance motion of the large and heavy Ba^{2+} requires a critical tunnel environment like the empty square tunnel. As revealed by the above structural analysis for the $Ba_{0.22}TaO_{2.72}$, the $(TaO)^{3+}$ incorporation into the pentagonal tunnel results in expanded neighboring square tunnels. In contrast with the $(TaO)^{3+}$-free T1 phase $Ba_{0.4}TaO_{2.9}$, the expansion of square tunnels arising from the $(TaO)^{3+}$ incorporation could benefit the Ba^{2+} migration in the $(TaO)^{3+}$-containing T2 phase $Ba_{0.22}TaO_{2.72}$.

The bulk conductivity of $Ba_{0.22}TaO_{2.72}$ varied within $\sim10^{-6}$–10^{-4} S/cm, with an activation energy of 0.665(2) eV over the 400–900 °C range (Figure 7). Above 550 °C, the bulk conductivity of $Ba_{0.22}TaO_{2.72}$ is ~1–4 orders of magnitude higher than that for the fully occupied stoichiometric TTB $Ba_6GaTa_9O_{30}$ pellet, showing typical electronic insulator behavior with higher activation energy, 2.02(3) eV. As both $Ba_{0.22}TaO_{2.72}$ and $Ba_{0.4}TaO_{2.9}$ pellets have low, but comparable, densities (~75% theoretical density due to their low sinterability), the lower permittivity for the $Ba_{0.22}TaO_{2.72}$ material can be likely ascribed to the $(TaO)^{3+}$ incorporation into the pentagonal tunnel, given that both materials contain comparable global cation deficiency in the tunnels (Figure 5a); i.e., the existence of $(TaO)^{3+}$ units in pentagonal tunnels and the local relaxation of the octahedral framework around the alternate Ta-O rows may affect the dielectric polarization.

The structural chemistry in the defect TTB solid solution and the spontaneous phase separation elucidated here is highly pertinent to other pentagonal-tunnel-related structures derived from the basic perovskite parent by a rotation of octahedral units,[11] for example, the orthorhombic $A_4B_2M_{10}X_{30}$-[13] and $A_2B_6M_{10}X_{30}$-,[36] the tetragonal $A_{12}B_6C_2M_{36}X_{108}$- (C denotes sites in hexagonal tunnels),[37] and the orthorhombic $A_4B_{10}M_{18}X_{54}$-type[14] corner-sharing octahedral tungsten bronzes and monoclinic $A_2B_7C_1M_{16}X_{47}$-type[38] mixed corner- and edge-sharing octahedral tungsten bronzes (Figures S3–S8 in the Supporting Information). Among them, the orthorhombic $A_2B_6M_{10}X_{30}$-, tetragonal $A_{12}B_6C_2M_{36}X_{108}$-, and monoclinic $A_2B_7C_1M_{16}X_{47}$-type tungsten bronzes free of alternate M and X rows in the pentagonal tunnels and the orthorhombic $A_4B_{10}M_{18}X_{54}$-type tungsten bronzes with alternate M and X rows in the pentagonal tunnels could also be interesting targets to examine. The exploitation of nonstoichiometric chemical defects may enable innovative tuning of structure–property correlations in the family of pentagonal-tunnel-containing octahedral framework structures.

CONCLUSIONS

In summary, defect TTB $Ba_{0.5-x}TaO_{3-x}$ oxide structures elucidated here reveal how the TTB structure adapts to a wide range of cationic and anionic defect stoichiometries. The slight nonstoichiometry in $Ba_{0.5-x}TaO_{3-x}$ (x = 0–0.1) forms the framework oxygen and tunnel cation deficiencies in the TTB structure. The highly nonstoichiometric TTB $Ba_{0.5-x}TaO_{3-x}$ ($0.25 \leq x \leq 0.325$) structure is stabilized via interpolating Ba^{2+} cations with alternating Ta-O rows into the pentagonal tunnels. These two mechanisms lead to an unexpected phase separation into two closely related $(TaO)^{3+}$-free and $(TaO)^{3+}$-containing TTB phases in $Ba_{0.5-x}TaO_{3-x}$ within the intermediate stoichiometric range of $0.1 < x < 0.25$. The $(TaO)^{3+}$-containing TTB phases exhibit variable $(TaO)^{3+}$ and Ba contents in the pentagonal tunnels with a maximum $(TaO)^{3+}$ content of 1/3. The incorporation of $(TaO)^{3+}$ into pentagonal tunnels and the resulting local relaxation of the octahedral framework for accommodating the $(TaO)^{3+}$ units in $Ba_{0.22}TaO_{2.72}$ emphasize the flexibility of the TTB octahedral framework and highlight its impact on the transport and polarization properties. The introduction of alternating M-O rows, such as the $(TaO)^{3+}$ units observed here in the pentagonal tunnels, could offer an extra freedom for manipulation of composition and property of the TTB materials. The flexible and tunable defect chemistry observed in the TTB $Ba_{0.5-x}TaO_{3-x}$ may be widely applicable to many other octahedral framework structures containing pentagonal tunnels.

ASSOCIATED CONTENT

Supporting Information

Electron diffraction patterns from the TTB superstructures observed in the $Ba_{0.22}TaO_{2.72}$ sample; z = 0.5 section of the difference Fourier map calculated using the TTB structural model on the laboratory XRD data for the $Ba_{0.22}TaO_{2.72}$; the refined structural parameters for $Ba_{0.22}TaO_{2.72}$ in the average structural model; the selected interatomic distances and the bond angles in TaO_n polyhedron for $Ba_{0.22}TaO_{2.72}$ in the site-split model; examples of octahedral framework structures containing pentagonal tunnels; and crystallographic information files in CIF format of the $Ba_{0.22}TaO_{2.72}$ for the average structure model and the site-split model. This material is available free of charge via the Internet at http://pubs.acs.org.

AUTHOR INFORMATION

Corresponding Authors

*E-mail: kuangxj@glut.edu.cn.
*E-mail: mathieu.allix@cnrs-orleans.fr.

Notes

The authors declare no competing financial interest.

ACKNOWLEDGMENTS

This work is supported by the National Natural Science Foundation of China (No. 21101174). X.K. thanks Guilin University of Technology and the MOE Scientific Research Foundation for Returned Scholars for the Start-up Fund. Use of the Advanced Photon Source (beamline 11-BM) at Argonne National Laboratory was supported by the U.S. Department of Energy under Contract No. DE-AC02-06CH11357. The authors acknowledge the support of the Laboratoire Léon Brillouin at CEA/Saclay (beamline 3T2) for the neutron beamtime. We also thank Dr. Jiyong Yao (Technical Institute of Physics and Chemistry) for the help on the SHG measurement.

REFERENCES

(1) Catlow, C. R. A.; James, R. *Nature* **1978**, *272*, 603.
(2) Maier, J. *Angew. Chem., Int. Ed.* **1993**, *32*, 313.
(3) Rao, C. N. R.; Gopalakrishnan, J. *New Directions in Solid State Chemistry*, 2nd ed.; Cambridge University Press: Cambridge, U.K., 1997; p 234.
(4) Li, M. R.; Kuang, X. J.; Chong, S. Y.; Xu, Z. L.; Thomas, C. I.; Niu, H. J.; Claridge, J. B.; Rosseinsky, M. J. *Angew. Chem., Int. Ed.* **2010**, *49*, 2362.
(5) Kuang, X. J.; Green, M. A.; Niu, H.; Zajdel, P.; Dickinson, C.; Claridge, J. B.; Jantsky, L.; Rosseinsky, M. J. *Nat. Mater.* **2008**, *7*, 498.
(6) Konysheva, E.; Suard, E.; Irvine, J. T. S. *Chem. Mater.* **2009**, *21*, 5307.
(7) Raveau, B. *Angew. Chem., Int. Ed.* **2013**, *52*, 167.
(8) Dickens, P. G.; Whittingham, M. S. *Q. Rev., Chem. Soc.* **1968**, *22*, 30.
(9) Yamauchi, K.; Picozzi, S. *Phys. Rev. Lett.* **2010**, 105.
(10) Chi, E. O.; Gandini, A.; Ok, K. M.; Lei, Z.; Halasyamani, P. S. *Chem. Mater.* **2004**, *16*, 3616.
(11) Hyde, B. G.; O'Keeffe, M. *Acta Crystallogr., Sect. A.* **1973**, *29*, 243.
(12) Bonner, W. A.; Grodkiewicz, W. H.; Van Uitert, L. G. *J. Cryst. Growth* **1967**, *1*, 318.
(13) Wang, L.; Sakka, Y.; Rusakov, D. A.; Mozharivskyj, Y.; Kolodiazhnyi, T. *Chem. Mater.* **2011**, *23*, 2586.
(14) Ohsato, H. *J. Eur. Ceram. Soc.* **2001**, *21*, 2703.
(15) Arnold, D. C.; Morrison, F. D. *J. Mater. Chem.* **2009**, *19*, 6485.
(16) Ohsato, H. *J. Eur. Ceram. Soc.* **2007**, *27*, 2911.
(17) Galasso, F.; Katz, L.; Ward, R. *J. Am. Chem. Soc.* **1959**, *81*, 5898.
(18) Layden, G. K. *Mater. Res. Bull.* **1967**, *2*, 533.
(19) Vanderah, T. A.; Roth, R. S.; Siegrist, T.; Febo, W.; Loezos, J. M.; Wong-Ng, W. *Solid State Sci.* **2003**, *5*, 149.
(20) Kovba, L. M.; Lykova, L. N.; Paromova, M. V.; Lopato, L. M.; Shevchenko, A. V. *Russ. J. Inorg. Chem.* **1977**, *20*, 2845.
(21) Cao, J.; Yu, X. D.; Kuang, X. J.; Su, Q. *Inorg. Chem.* **2012**, *51*, 7788.
(22) Rietveld, H. M. *J. Appl. Crystallogr.* **1969**, *2*, 65.
(23) Coelho, A. A. *TOPAS Academic V4*; Coelho Software: Brisbane, Australia, 2005.
(24) Petricek, V.; Dusek, M.; Palatinus, L. *Jana2006: The Crystallographic Computing System*; Institute of Physics: Praha, Czech Republic, 2006.
(25) Brown, I. D.; Altermatt, D. *Acta Crystallogr., Sect. B* **1985**, *41*, 244.
(26) Sleight, A. W. *Acta Chem. Scand.* **1966**, *20*, 1102.
(27) Krumeich, F.; Geipel, T. *J. Solid State Chem.* **1996**, *124*, 58.
(28) Sears, V. F. *Neutron News* **1992**, *3*, 26.
(29) Evans, I. R.; Howard, J. A. K.; Evans, J. S. O. *J. Mater. Chem.* **2003**, *13*, 2098.
(30) Irvine, J. T. S.; Sinclair, D. C.; West, A. R. *Adv. Mater.* **1990**, *2*, 132.
(31) Montemayor, S. M.; Alvarez Mendez, A.; Martínez-de La Cruz, A.; Fuentes, A. F.; Torres-Martínez, L. M. *J. Mater. Chem.* **1998**, *8*, 2777.
(32) Reisinger, S. A.; Leblanc, M.; Mercier, A. M.; Tang, C. C.; Parker, J. E.; Morrison, F. D.; Lightfoot, P. *Chem. Mater.* **2011**, *23*, 5440.
(33) Krumeich, F. *Acta Crystallogr., Sect. B* **1998**, *54*, 240.
(34) Andersson, S. *Acta Chem. Scand.* **1965**, *19*, 2285.
(35) Farrington, G. C.; Dunn, B. *Solid State Ionics* **1982**, *7*, 267.
(36) Lundberg, M. *Acta Chem. Scand.* **1965**, *19*, 2274.
(37) Yamazoe, N.; Kihlborg, L. *Acta Crystallogr., Sect. B* **1975**, *31*, 1666.
(38) Viswanathan, K.; Brandt, K.; Salje, E. *J. Solid State Chem.* **1981**, *36*, 45.